RESEARCH ARTICLE
doi.org/10.1002/elsa.202100151

Chemistry Europe
European Chemical Societies Publishing

Received: 2 September 2021
Revised: 22 December 2021
Accepted: 19 January 2022

Influence of carbon binder domain on the performance of lithium-ion batteries: Impact of size and fractal dimension

Anshuman Chauhan | **Ermek Asylbekov** | **Susanne Kespe** | **Hermann Nirschl**

Institute of Mechanical Process Engineering and Mechanics, Karlsruhe Institute of Technology, Karlsruhe, Germany

Correspondence
Anshuman Chauhan, Institute of Mechanical Process Engineering and Mechanics, Karlsruhe Institute of Technology, Kaiserstraße 12 76131 Karlsruhe, Germany.
Email: anshuman.chauhan@kit.edu

Funding information
Deutsche Forschungsgemeinschaft, Grant/Award Number: DFG GRK 2218/2

Abstract

A lithium-ion battery (LIB) cathode comprises three major components: active material, electrical conductivity additive, and binder. The combination of binder and electrical conductivity additive leads to the formation of composite clusters known as the carbon binder domain (CBD) clusters. Preparation of a LIB cathode strongly influences the dispersion of the above-mentioned constituents leading to the formation of distinct pore and electrical conduction networks. The resulting structure thus governs the performance of LIBs. The presence of CBD is essential for the structural integrity and sufficient electrical conductivity of the LIB cathode. However, CBD abundance in LIB cathodes leads to unfavorable gravimetrical and volumetrical consequences owing to its electrochemical inertness. Increasing CBD content adds to the weight of the LIBs, thus negatively impacting the energy density. Furthermore, increased electrical conductivity is won at a cost of ionic conductivity as CBD clusters breach the pore networks in the cathode microstructure. The following study establishes a link between the various possibilities of CBD cluster size and fractal dimension that may eventualize during the mixing process of slurry preparation to the resulting microstructural properties and hence to the performance of LIBs by means of idealized cathode geometries. Since the performance determining processes occur at the microstructural scale, which are often very tedious to study via experimental research, the study makes use of spatially resolving microstructural, numerical, simulations. The results demonstrate that the CBD cluster size has a strong influence on the cathode microstructure. The CBD cluster fractal dimension on the other hand displayed a minor influence on the structural properties of the cathode, and the size of the cluster primary particles was shown to be the dominant factor. Finally, performance evaluation simulations confirmed the trends seen in structural properties with changing cluster size and fractal dimension.

KEYWORDS
carbon binder domain, cathode microstructure, cell performance, conductivity, three-dimensional battery simulations

1 | INTRODUCTION

Carbon black is widely used as an electrical conductivity additive in lithium-ion battery (LIBs). Owing to the poor electrical conductivity of commonly used electrochemically active material, [1] the presence of such an additive is imperative. During the preparation of LIBs, by virtue of its high-specific surface area, carbon black dominates the interaction with the binder during the mixing process. This leads to the formation of composite clusters referred to in this work as carbon binder domain (CBD) clusters. These clusters build electrical connections within the slurry and impart gel-like characteristics to the suspension. The cathode slurry thus formed with particulate active material held together and onto the cathode current collector by composite clusters of CBD is electrically conductive and rheologically stable. [2] The ensuing drying of the slurry coated onto the current collector immobilizes the percolating network of CBD clusters responsible for current conduction in the cathode and a network of pores emerges. Subsequently, the dried coating undergoes compression during the calendering processes to improve its energy density and electrical conductivity. [3] Upon the assembly of LIBs, the pore network is ultimately filled with an electrolyte, which accounts for the transportation of lithium ions. The interdependent distribution of the pores space and the CBD clusters strongly influences the rate of electrochemical reactions taking place in the cathode and hence the performance of LIBs. Surplus CBD content leads to reduced pore space thus resulting in a deficiency of lithium ions at intercalation sites, reversibly a highly porous microstructure is incapable of meeting the current conduction demands essential at high discharge current rates. Hence, an optimal distribution of the two mentioned networks is essential to obtain high-performance cathodes.

Numerous attempts have been made at understanding how the combination of binder and electrical conductivity additives and their distribution affect LIBs. Conduction phenomena in carbon–polymer composites by means of electron tunneling was reported in Refs. [4–7]. Additionally, the decisive role played by binder in LIB electrodes was emphasized in Refs. [2] and [8]. In the aforementioned works, it was observed that the interaction of binder and carbon black in cathode slurries leads to the formation of composite clusters that enhanced electrical conductivity and structural integrity; however, surplus binder in the suspension was not immobilized by carbon black particles in the form of composite clusters and deposited itself on the surface of active material. This lead to a decrease in the electrical conductivity at contacts between active material particles and hindered the movement of lithium ions towards intercalation sites. Detailed influence of the CBD on microstructural characteristics such as specific active surface area and tortuosity was reported in Refs. [9], [10] and [11]. It is evident from these contributions that the CBD has a pronounced effect on the cathode microstructure. Likewise, CBD morphology [12] as well as its spatial distribution [13] was also reported to influence the impedance of LIB electrodes. A combined study of electric and ionic conduction phenomenon reported in Refs. [14] and [15] paved way to optimization studies of likes reported in Refs. [16] and [17]. Consequently, performance predictions based on structural characteristics as well as the interplay of conduction phenomena were reported in Refs. [18] and [19] applied to high-power and high-energy LIBs, respectively.

Even so, a comprehensive account of the influence of CBD on the structural properties, the conduction phenomena, and performance is scarce in contemporary literature. Additionally, implications of processes involved in the fabrication of LIBs have largely been overlooked in the case of numerical studies while modeling the CBD. Findings reported in Refs. [20] and [21] deliver insights about dispersion of slurry components from the mixing stage of LIB fabrication. Complementary to these findings, Forouzan et al. [22] and Rucci et al. [23] report the influence of drying on cathode slurries along with its impact on electrochemical performance. Finally, with the inclusion of the calendering process, studies such as Refs. [24] and [25] report the ability to computationally generate promising cathodes that can be utilized to study the effect of the cathode mesostructure on performance. Inspired from these works, in the framework of this study, possible cathode microstructures that may arise during the mixing process owing to the particulate nature of cathode slurries were realized with the help of idealized geometries. The idealized geometries in this context refer to a system of dense spherical particles comprising two components representing the active material and CBD, respectively. It is assumed that all the binder available in the cathode is integrated into the CBD, and no surplus binder remains in the system. The individual components have uniform shape and dimension. The active material, lithium nickel manganese cobalt oxide (NMC) has been modelled as smooth spheres with a diameter of 10 μm as is the case in contemporary numerical studies. [7,23,26] Unfortunately, a similar consensus does not exist for the size and shape of the

RESEARCH ARTICLE
doi.org/10.1002/elsa.202100151

CBD. To begin with, in situ measurement of CBD clusters in fabricated cathodes is extremely arduous. In addition, owing to the randomness involved in the process of mixing, the search for a dominant shape is frivolous. Thus, measurements carried out for quality control of cathode suspensions reported in Ref. [20] were used as the basis to determine the CBD size d_s. Herein, carbon black particle diameters are reported under two categories: permanently bound aggregates in the range 0.05–0.9 μm and agglomerates in the range 1–9 μm. Owing to the increasing computational effort with decreasing particle size, the CBD diameter was restricted to the category of agglomerates. Finally, in order to account for the shape of the CBD clusters, fractal dimension d_f ranging from 1.8 to 2.4 along with a change in the primary particle size d_p from 1 to 2 μm was deployed. This description has been inspired from the characterization of carbon black aggregate shapes reported in Refs. [27, 28].

The results of the investigations made in this work have been split into two substudies reporting the impact of CBD size and fractal dimension, respectively. For the purpose of these studies, the idealized cathode geometries were transformed into half-cell computational domains with periodic boundaries in the in-plain direction with a dimension of $30 \times 30 \times 58\,\mu\text{m}^3$ and $30 \times 30 \times 40\,\mu\text{m}^3$ correspondingly. The half-cells were at first characterized by the numerical evaluation of structural properties: tortuosity, specific active surface area, and effective electrical conductivity and then followed by, electrochemical discharge simulations under galvanostatic operation conditions and varying discharge rates. Based on the half-cell potential progression obtained from the spatially resolving simulations with reference to a lithium metal anode, performance could be evaluated. It was found that within the investigated domain, CBD size has a significant impact on the cathode microstructure and hence the resulting performance. Furthermore, opposing trends were observed in structural characteristics for electrical and ionic conductivity, demonstrating that the former is won at the cost of the latter. Consequently, it was observed that while half-cells with larger CBD size $d_s \geq 2$ exhibited evidently better performance at lower discharge rates, the relative gap in performance to half-cells with smaller CBD size reduced with increasing discharge rate. Indicating that at higher current rates additional capacity loss mechanisms that influence cathode performance come into play.

2 | NUMERICAL METHOD

This section discusses in detail the generation of the idealized microstructures, the computational models involved in the characterization of the half-cell geometries and the spatially resolving electrochemical model used to evaluate performance. The following subsections have been presented in the chronological order.

2.1 | Idealized microstructure generation

The building block of the cathode microstructures investigated in this contribution was randomly arranged stack of dense, smooth, spherical particles. These microstructures were generated by means of discrete element method (DEM) simulations, carried out using the open-source code LIGGGHTS [29]. The DEM simulations carried out within the scope of this work, serve only as a means of mimicking the spatial distribution of the cathode components. Hence, the detailed modeling of the particle–particle or particle–wall interactions necessary to describe the transient behavior of cathode slurries have not been included. For the generation of a stack of particles distributed randomly over a given thickness, a fixed number of particles of two species namely active material and CBD were randomly inserted into a simulation box and then allowed to drop and roll with periodic boundaries in the x- and y-directions and a fixed wall at $z = 0$. The particles fall from their initial position under the influence of an external acceleration in the negative z-direction and undergo collisions. The movement of the particles was calculated based on the conservation of momentum, and the contact forces were modeled by the Hertz–Mindlin model [30]. The contact configuration thus generated between the active material and CBD componentis qualitatively similar to the one shown to best reproduce impedance measurement data in Ref. [12]. In the case of the size substudy, each individual particle of the species CBD represents a CBD cluster, whereas for the fractal dimension substudy a group of particles generated by means of the tunable dimension method constitute the same. Details of the modeling of the CBD cluster geometries inspired by the characterization of carbon black aggregate shapes with the help of fractal dimension can be found in Ref. [21].

The size of the simulation box was set to $30 \times 30\,\mu$m in the in-plain direction based on the studies on unit cell size implication on structural properties reported in Ref. [31]. In order to fix the cathode dimension in the z-direction, the particle stack was subjected to uniaxial compression by means of a wall moving in the negative z-direction, once the stack of particles had settled down and a state of minimum energy had been reached as demonstrated in Ref. [31], thus adjusting the volume fractions of the active, inactive, and the pore component. The electrodes were modeled to be 58 μm thick for the size substudy and 40 μm thick for the investigation of fractal dimension. In the following steps, these stacks of particles were transformed into half-cells as shown in Figure 1. In order to save computational cost, only particles whose center lie within

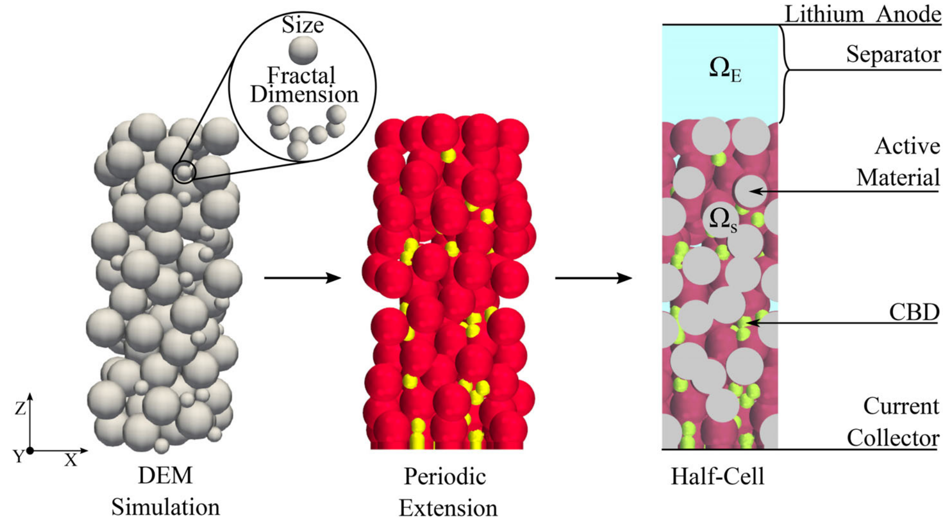

Figure 1 Generation of idealized half-cell geometries

Table 1 Resulting component volume fractions from DEM simulations

	Active material (%)	CBD (%)	Porosity (%)
Size I	57 ± 0.7	9 ± 0.8	34 ± 1.4
Size II	57 ± 0.8	9 ± 0.8	34 ± 1
Fractal dimension (Dp = 1 μm) I	58 ± 0.4	9 ± 0.4	33 ± 0.6
Fractal dimension (Dp = 1 μm) II	58 ± 0.1	9	33 ± 0.9
Fractal dimension (Dp = 2 μm) I	57 ± 1.0	8 ± 0.2	35 ± 1
Fractal dimension (Dp = 2 μm) II	58	8 ± 0.1	34 ± 0.2

the simulation box were considered during the DEM simulations, thus to generate periodically continuous cathode geometries, the resulting particle stacks were periodically extended to include particles lying outside the simulation box but projecting into it. This was followed by the trimming of particle stacks along the dimension of the simulation box thus, generating the periodic cathode domain Ω_S. Finally the pore volume within the cathode as well an additional thickness of 25 μm representing the separator, sitting on top of the cathode domain were filled to the dimension of the simulation box, resulting in the formation of the electrolyte domain Ω_E. The randomized initial insertion of particles in DEM simulations is regulated with a pseudo-random number generation strategy starting from an arbitrarily chosen prime number known as a seed. Hence, in order to rule out the effect of the initialization of particles, a set of two microstructures labeled with roman numerals I and II, each with a different seed was produced for each size and fractal dimension investigated. The volume fractions of the individual components and the porosity were held constant to ensure comparability. Table 1 shows the achieved volume fractions of individual components at the end of the particle simulations. The meshing of the two computational regions thus generated was carried out in Simcenter STAR-CCM+ ®.

2.2 | Characterization

In order to quantify the influence of size and fractal dimension on the cathode microstructure, a numerical evaluation of the structural properties was carried out. Details of the models used and the significance of the individual properties have been discussed below. All the numerical models were implemented using the finite volume method based on the open source code OpenFOAM, Version 7.

2.2.1 | Tortuosity, porosity, and specific active surface area

In this study, tortuosity has been used as a means to quantify the quality of the cathode pore structure. In this context, as stated in Ref. [33], tortuosity describes the nature of a three-dimensional pore system, interrelating porosity and diffusion phenomenon. Based on the relationship between tortuosity τ, porosity ϵ and effective diffusion coefficient D_E^{eff}, Equation (2.3), Kespe et. al. [34] implemented a numerical scheme for the evaluation of effective diffusion coefficient and hence the tortuosity. The model equations are summarized in Table 2.

Table 2 Model equations for determination of tortuosity

Cathode, $\Omega_S = \Omega_S^{AM} \cup \Omega_S^{CBD}$	**Electrolyte, $\Omega_E = \Omega_E^{REST} \cup \Omega_E^{SEP}$**	
-	$\nabla \cdot (D_E \cdot \nabla c_E) = 0$	(2.1)
-	$\nabla c_E \cdot \vec{n}_E = 0$ on $\partial\Omega_{E,S}$	(2.2)
-	$D_E^{eff} = D_E \frac{\epsilon}{\tau}$[32]	(2.3)

Herein, D_E is the local diffusion constant, c_E the local electrolyte concentration, $\vec{n}_E$ the outward normal, and $\partial\Omega_{E,S}$ the contact boundary between the electrolyte and cathode. The numerical scheme assumes a unit concentration gradient over the thickness of the electrolyte, leading to the evolution of a species flux. Following the periodic nature of the microstructures, the periodic boundary condition was applied in the x- and y-directions. The magnitude of the mass flux, thus obtained at the current collector $\dot{N_{cc}}$ reveals the effective diffusion coefficient of the microstructure according to the equation:

$$D_E^{eff} = \dot{N}_{cc} \frac{1}{c_E^{sep} - c_E^{cc}} \frac{H}{\Delta x \Delta y} \tag{1}$$

wherein c_E^{sep} and c_E^{cc} represent the surface-averaged concentration at the bottom surface of the separator and the current collector, respectively. The electrode thickness is represented as H and Δx and Δy denote the lateral dimensions of the investigated half-cell in the x and y-directions. With a known porosity and local diffusion coefficient, which were set constant over the variants to ensure comparability, the tortuosity was calculated by Equation (2.3). Higher tortuosity indicates reduced effective diffusion capability of the pore system and thus poor ionic conductivity. As discussed further in Section 3.1, increased tortuosity was also accompanied by decreased specific active surface area S_v. Here, specific active surface area refers to the active microstructural area available per unit volume for intercalation. As the tortuosity rises with increasing filling of the pore space, more CBD clusters come in contact with active material particles leading to reduction of the overall freely available active surface area. Reduction in specific active surface is detrimental for LIBs as it leads to sharper electrochemical gradients for similar operating conditions. Further elaboration on the phenomenon can be found in Section 3.1.

2.2.2 | Effective electrical conductivity

As a means of quantifying the electrical conductivity within the cathode, the globally measurable, macroscopic property, effective electrical conductivity has been utilized. The investigations thus carried out are based on similar principles as reported in Refs. [16] and [17]. The numerical implementation was carried out by Kespe et. al [35]. The governing equations are tabulated in Table 3. The model presented is derived from the measurement of electrical conductivity in the direction perpendicular to the electrode. For this purpose, the top most layer of the cathode is set to have a potential of 1 V and the bottom surface in contact with the current collector is held at 0 V potential. Thus, a unit potential difference $\Delta\phi$ is established leading to an electrical current I_{cc}, at the current collector. The in-plain directions are coupled periodically and the current restricted to the cathode domain by means of Equation (3.2). Herein, $\vec{n}_S$ represents the outward normal and $\partial\Omega_{S,E}$ the contact boundary between the cathode and electrolyte. Under the stated boundary conditions, a unique solution for the charge balance, Equation (3.1) , where κ_S represents the local constant electrical conductivity and ϕ_S the local potential, can be reached. Finally, upon evaluation of the current achieved at the current collector and the dimension of unit cell (H, Δx, and Δy) stated in the previous section, the effective electrical conductivity in the z-direction can be calculated as

$$\kappa_S^{eff} = \frac{I_{cc}}{\Delta\phi} \frac{H}{\Delta x \Delta y}. \tag{2}$$

2.3 | Performance evaluation

The basis for the electrochemical evaluation presented in this work is the numerical model developed by Kespe et al. [36] The model was previously used in the investigation of spatial distribution of electrical conductivity within the cathode microstructure [35] as well as in the spatially resolved numerical investigation of active material porosity [37] and roughness [38]. Two non-overlapping domains namely the solid cathode Ω_S and the liquid electrolyte Ω_E comprise the half-cell computational domain used by the model. The periodic boundary condition couples both the domains in the plain and isothermal operation at $T = 298$ K is assumed. Within the framework of this publication, all cathodes constitute of an active subdomain Ω_S^{AM}, composed of NMC and a passive subdomain Ω_S^{CBD}, composed of the combination of carbon black and binder. In order to hinder the lithium transportation within the passive subdomain, the diffusion coefficients in the respective

Table 3 Model equations for determination of effective electrical conductivity

Cathode, $\boldsymbol{\Omega_S = \Omega_S^{AM} \cup \Omega_S^{CBD}}$		**Electrolyte, $\boldsymbol{\Omega_E = \Omega_E^{REST} \cup \Omega_E^{SEP}}$**
$\nabla \cdot (\kappa_S \cdot \nabla \phi_S) = 0$	(3.1)	-
$\nabla \phi_S \cdot \vec{n_S} = 0$ on $\partial\Omega_{S,E}$	(3.2)	-

Table 4 Governing equations for the spatially resolving electrochemical model on the microscale

Cathode, $\boldsymbol{\Omega_S = \Omega_S^{AM} \cup \Omega_S^{CBD}}$		**Electrolyte, $\boldsymbol{\Omega_E = \Omega_E^{REST} \cup \Omega_E^{SEP}}$**	
$\frac{\partial c_S}{\partial t} = \nabla \cdot (D_S \cdot \nabla c_S)$	(4.1)	$\frac{\partial c_E}{\partial t} = \nabla \cdot (D_E \cdot \nabla c_E) + \frac{t_+^0}{F} \nabla \cdot \vec{i_E}$	(4.2)
$\vec{i_S} = \kappa_S \cdot \nabla \phi_S$	(4.3)	$\vec{i_E} = -\kappa_E \cdot \nabla \phi_E + \frac{2RT\kappa_E}{F}(1 - t_+^0)\ln(c_E)$	(4.4)
$\nabla \cdot \vec{i_S} = 0$	(4.5)	$\nabla \cdot \vec{i_E} = 0$	(4.6)
$\vec{i_{BV}} = \begin{cases} 2 \cdot F\, k_{BV}(c_S^{max} - c_S)^{\alpha_a}(c_S)^{\alpha_c}(c_E)^{\alpha_a} \sinh(\frac{\alpha F \eta}{2RT}) & \text{on } \partial\Omega_{S,E}^{AM} \\ 0 & \text{on } \partial\Omega_{S,E}^{CBD} \end{cases}$ (4.7)			
$\eta = \phi_S - \phi_E - U_{eq}$ (4.8)			
$\vec{i_{BV}} \cdot \vec{n_S} = -\vec{i_E} \cdot \vec{n_E}$ (4.9)			

subdomains have been set such that $D_S^{CBD} << D_S^{AM}$. The liquid electrolyte has been parameterized based on the completely dissociated conducting salt, lithium hexafluorophosphate ($LiPF_6$) in a solvent consisting of a mixture of ethylene carbonate (EC) and ethyl methyl carbonate (EMC) [39]. In each of the half-cells, the separator is modeled with the help of effective transport properties as a subdomain Ω_E^{SEP} of constant thickness within the electrolyte domain. The constituent equations of the model are summarized in Table 4.

The pillars of the model are charge and mass conservation in both domains and an electrochemical coupling of the two that dictates the kinetics. Equations (4.1) and (4.2) represent the mass conservation in the respective domains. The charge conservation on the other hand is given by Equations (4.5) and (4.6). Herein, $\vec{i_E}$ denotes the ionic current density, $\vec{i_S}$ the electronic current density, κ_S the solid electrical conductivity, and κ_E the ionic conductivity. In case of the electrolyte, the ionic conductivity κ_E and the diffusion coefficient D_E were modeled to be dependent on the electrolyte concentration c_E, according to the relations published by Less et al. [39]:

$$\begin{aligned}\kappa_E = &-2.39 \times 10^{-11} \cdot {c_E}^4 + 1.21 \times 10^{-7} \cdot {c_E}^3 \\ &-2.89 \times 10^{-4} \cdot {c_E}^2 + 0.32 \cdot c_E - 2.789. \qquad (3)\end{aligned}$$

$$\begin{aligned}D_E = &\ 1.2 \times 10^{-21} \cdot {c_E}^4 - 6.5 \times 10^{-18} \cdot {c_E}^3 + 1.14 \times 10^{-14} \cdot \\ &{c_E}^2 - 8.06 \times 10^{-12} \cdot c_E + 2.24 \times 10^{-9}. \qquad (4)\end{aligned}$$

Finally, a Butler–Volmer type [40] electrochemical kinetic relation equation (4.7) couples the two domains via the intercalation current density denoted as $\vec{i_{BV}}$, hereunder F denotes the Faraday's constant and R the universal gas constant. The intercalation current density was set to zero at the partial boundary $\partial\Omega_{S,E}^{CBD}$ of the passive subdomain to ensure its electrochemical inactivity. Additionally, Equation (4.9) accounts for continuity, wherein $\vec{n_S}$ and $\vec{n_E}$ represent the outward normals of the cathode and electrolyte domain, respectively. The anode was considered to be composed of metallic lithium, and the cathode current collector was modeled to be impermeable to lithium ions with the help of appropriate boundary conditions. The model parameters used in this work are summarized in Table 5. In order to evaluate performance from the electrochemical simulations, the half-cell potential evaluated with respect to the lithium metal anode was plotted in form of discharge curves along the depth of discharge (DOD). The DOD is an indication of the state of charge of the battery and is evaluated using the solid concentration c_S following the equation:

$$DOD = \frac{\int (c_S(\vec{x}, t) - c_{S,ref})}{\int (c_{S,max} - c_{S,ref})}. \qquad (5)$$

Under galvanostatic discharge conditions, LIBs are discharged up to a cut-off voltage (COV) to avoid degradation of its components [41]. Cut-off voltage serves as an indicator for the end of the discharge cycle and lies at 3.4 V for this study. As suggested by Kespe et. al [36], based on the $DOD(COV)$ achieved by a half-cell at the COV, its utilizable capacity can be evaluated with respect to the theoretical maximum capacity achieved under equilibrium operation conditions, $DOD_{eq}(COV)$. The basis for the equilibrium operation condition has been derived

Table 5 Parameters for the spatially resolving electrochemical model on the microscale

	Value	Unit	Reference
Cathode			
Active material electrical conductivity, κ_S^{AM}	1	S m^{-1}	[1]
CBD electrical conductivity, κ_S^{CBD}	100	S m^{-1}	[8]
Active material coefficient of diffusion,D_S^{AM}	4.3032×10^{-14}	m^2 s^{-1}	[19]
CBD coefficient of diffusion, D_S^{CBD}	1×10^{-20}	m^2 s^{-1}	[31]
Initial cathode potential, $\phi_{S,ref}$	4.3	V	[12]
Active material initial lithium concentration, $c_{S,ref}^{AM}$	18,409.57	mol m^{-3}	[19]
Active material maximum lithium concentration, $c_{S,max}^{AM}$	50,451	mol m^{-3}	[19]
CBD lithium concentration, $c_{S,ref}^{CBD}$	0	mol m^{-3}	[31]
Equilibrium potential, U_{eq}	Equation (6)	V	[19]
Electrolyte			
Electrical conductivity ,κ_E	Equation (3)	S m^{-1}	[39]
Coefficient of diffusion, D_E	Equation (4)	m^2 s^{-1}	[39]
Initial electrolyte potential at anode surface, $\phi_{E,ref}$	0	V	[12]
Transfer number, t_+^0	0.4	-	[39]
Initial lithium concentration, $c_{E,ref}$	1000	mol m^{-3}	[34]
Separator			
Porosity ,ϵ_{sep}	0.5	-	[31]
Tortuosity, τ_{sep}	1.5	-	[31]
Buttler–Volmer kinetics			
Butler–Volmer reaction rate constant ,k_{BV}	1.4693×10^{-6}	A $m^{-2.5}$ $mol^{-1.5}$	[19]
Cathodic apparent transfer coefficient, α_c	0.5	-	[19]
Anodic apparent transfer coefficient, α_a	0.5	-	[19]
Overpotential, η	Equation (4.8)	-	-

from the equilibrium potential U_{eq} of NMC measured by Kremer et al. [19] denoted by the relation:

$$\begin{aligned} U_{eq} &= 13.4905 - 10.96038 \cdot c_S + 8.203617 \cdot c_S{}^{1.358699} \\ &- 3.10758 \times 10^{-6} \cdot e^{(127.1216 \cdot c_S - 114.2593)} \\ &- 7.033556 \cdot c_S^{-0.03362749} \end{aligned} \quad . \tag{6}$$

Hence the performance gauging parameter utilizable capacity can be evaluated as a percentage of the theoretical maximum capacity with the relation:

$$UC = \frac{DOD(COV)}{DOD_{eq}(COV)} \cdot 100. \tag{7}$$

3 | RESULTS AND DISCUSSION

The results and entailing discussion of the aforementioned substudies on size and fractal dimension, respectively, have been presented in detail in the following sections.

3.1 | Size

Figure 2 shows half-cell geometries encompassing the complete domain $1 \le d_s \le 9$ μm, of the investigated CBD diameter for the size substudy. A visual inspection of the geometries reveals that with decreasing diameter the CBD dispersion increases. The consequences of this change on the structural characteristics of the half-cells can be observed in Figure 3. The error bars in the figure represent the minimum and maximum values obtained, respectively, for a given CBD diameter and the solid line connecting the average values over the entire range shows the trend. It can be seen that, with decreasing diameter the tortuosity remains constant in the range $2 \le d_s \le 9$ μm as shown in Figure 3b on the left axis, with a maximum change of 8%. However, a sharp increase is observed as the diameter becomes further smaller. This steep shift can be explained by the fact that with decreasing diameter, there is an exponential increase in the number of CBD clusters, from 1396 CBD clusters of $d_s = 2\,\mu$m to 11,166 CBD clusters of $d_s = 1\,\mu$m that comprise the same volume fraction in the half-cell. Owing to their small size, these

RESEARCH ARTICLE
doi.org/10.1002/elsa.202100151

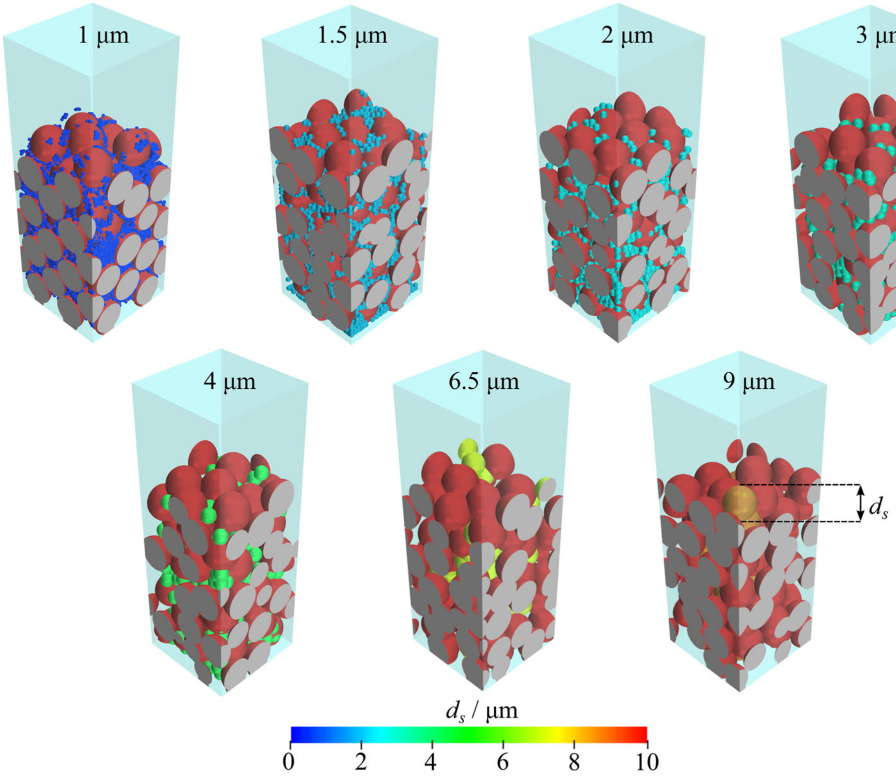

Figure 2 Idealized half-cell geometries of the CBD size variants with variation in CBD diameter d_s

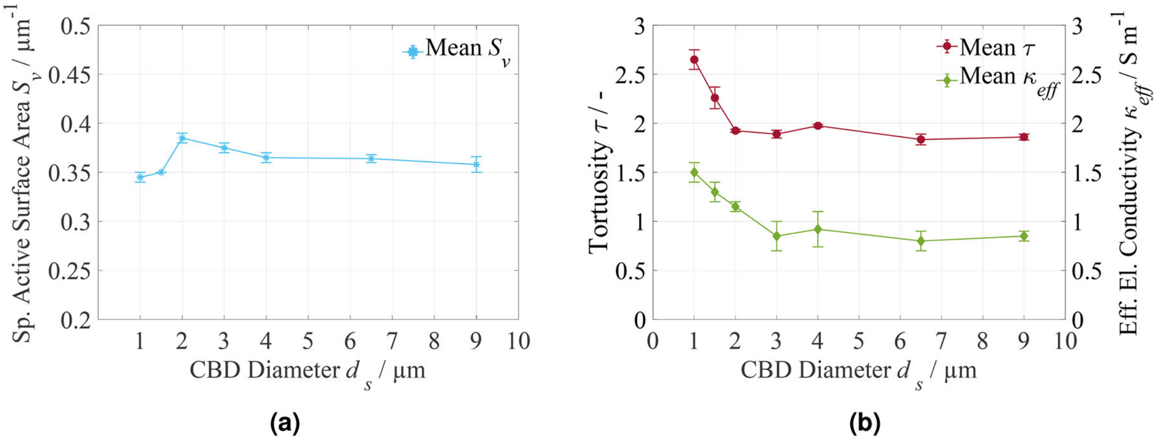

Figure 3 Structural characterization of the CBD size variants

CBD clusters seep into the pore networks, thus breaching percolating pathways of the pore network and hence increasing tortuosity and reducing ionic conductivity. On the contrary, the higher dispersion of the smaller CBD clusters leads to an improvement in the effective electrical conductivity κ_{eff} as shown on the right axis of Figure 3b. Similar to the trend in tortuosity, the effective electrical conductivity remains constant and close to the absolute electrical conductivity of the active material, that is, 1 S m^{-1} in the domain $2 \leq d_s \leq$,9 μm. However, increasing number of interparticle contacts initiated by the growing number of clusters, enhances the electrical connections in the cathode microstructure as the diameter is decreased further. Therefore, the electrical and ionic conductivities of cathode microstructures are strongly interconnected and gains in the former compromise the latter.

Finally, as shown in Figure 3a, the specific active surface area gradually increases with decreasing diameter from $d_s = 9\ \mu$m up to $d_s = 2\ \mu$m but, upon a further reduction in diameter a drastic decline in the specific active surface

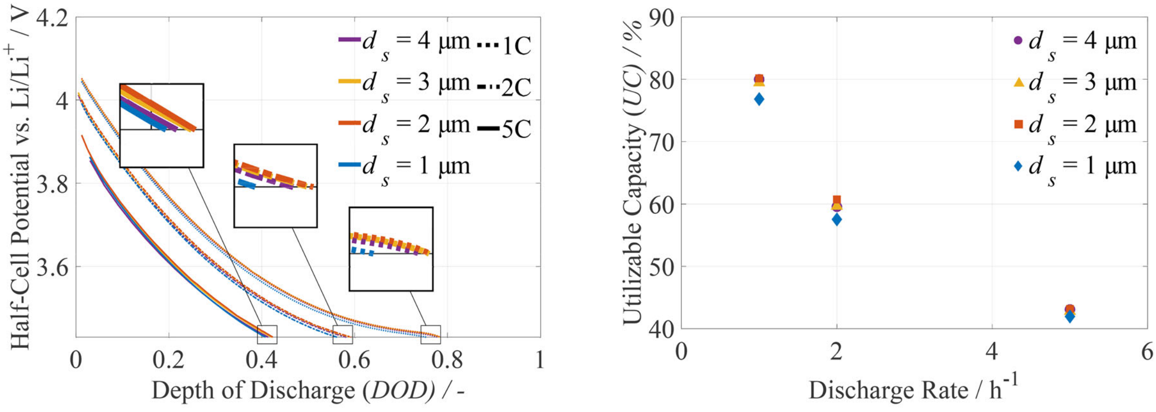

(a) **(b)**

Figure 4 Performance evaluation of the chosen CBD size variants

area is observed. The initial increase in active surface per unit volume with decreasing diameter can be accounted for by the decreasing contact area between individual CBD clusters and the active material caused by the reduced cluster size. Although the number of CBD clusters increases with decreasing diameter, the reduced contact area per cluster dominates until $d_s = 2\ \mu$m. Upon further reduction, the exponential increase in the number of contacts caused by the exponentially rising number of CBD clusters outweighs the decreased contact area of an individual cluster, leading to an overall loss in the specific active surface area and hence diminishing available intercalation sites.

As indicated earlier, the performance evaluation was carried out by means of spatially resolving microstructural numerical simulations. Figure 4 summarizes the results of these investigations. Only the size domain, wherein significant effects in the structural characterization were observed, was chosen, that is, $1 \leq d_s \leq 4\,\mu$m. All simulations were carried out under galvanostatic discharge conditions. The C-rates of 1C, 2C, and 5C were chosen so as to represent a wide range of commonly found discharge currents in the datasheets of commercial cells. Here, the C-rate is a measure of the discharge rate with respect to the maximum battery capacity. Figure 4a illustrates the discharge curves for the chosen variants across the different discharge current rates. It can be observed that the idealized half-cell with $d_s = 2\,\mu$m exhibits the highest half-cell potential over the entire discharge process and across all discharge rates, the half-cell variant with $d_s = 1\,\mu$m is worst among all the variants and the variants with $d_s = 3\,\mu$m and $4\,\mu$m are hard to differentiate from one another. This observation can be elucidated by the trends observed in the structural characterization of the half-cells. The increased active surface area and better pore connectivity (reduced tortuosity) for the $d_s = 2\,\mu$m variant leads to lower levels of intercalation current densities $\|\vec{i_{BV}}\|$ for same total discharge current in the half-cell. Lower $\|\vec{i_{BV}}\|$ in-turn implies that the half-cell can operate at a lower overpotential η (see Equations 4.7 and 4.8). Hence, resulting in higher half-cell potential over the entire depth of discharge. In contrast, the $d_s = 1\,\mu$m variant experiences higher current densities and higher overpotentials, resulting in a reduced potential measured across the half-cell. The findings correlate with similar observations made in Ref. [18]. Wherein, reduction in capacity was observed upon reduction in specific active surface area and rising tortuosity. Finally, the relative invariance in the structural properties of variants $d_s = 3\,\mu$m and $4\,\mu$m results in similar overpotentials and half-cell potentials.

In Figure 4b, the chosen performance metric, that is, the utilizable capacity has been plotted over the investigated discharge rates. The *UC* is evaluated with respect to the equilibrium operation condition of the half-cell thus it decreases with increasing current for all variants as shown in the figure, due to the rising over-potential. Complementary to what was observed in Figure 4a, it can been seen that $d_s = 2\,\mu$m variant has the highest utilizable capacity, the $d_s = 1\,\mu$m variant the lowest across all discharge rates and the variants with $d_s = 3\,\mu$m and $4\,\mu$m remain indifferentiable. The additional information supplied from the figure lies in the scaling of the utilizable capacity of the variants with changing discharge rate. It can be observed that the relative difference in the *UC* of the $d_s = 1\,\mu$m and $d_s = 2\,\mu$m variants shrinks with increasing discharge rate. The apparent shrink from 5% to 2% can be accounted for on the one hand by higher effective electrical conductivity of the former, leading to reduced electronic resistance which, was also shown to improve capacity in Ref. [42]. On the other hand, following the study of Du et al.[43], a

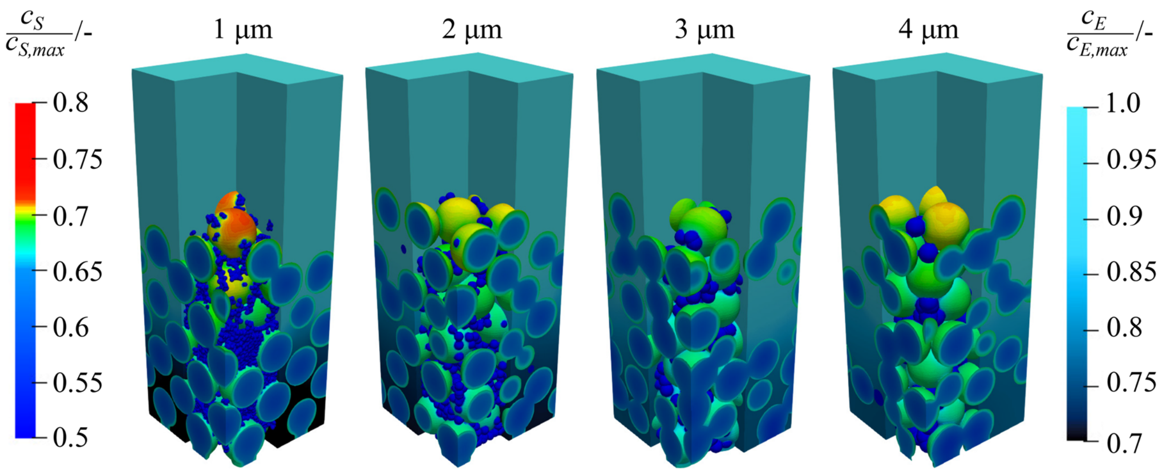

Figure 5 Relative lithium concentration distribution in the cathode and electrolyte domain of the selected CBD size variants after 310 s of galvanostatic discharge at 5C

purely diffusion-limited operation prevails for NMC particles subjected to high discharge rates implying that at the discharge rate of 5C the utilizable capacity of all the variants is limited by their solid-state diffusion.

In order to reveal further insights into the various phenomenon that influence half-cell performance, the resolved lithium concentration field in the cathode and electrolyte domains are depicted in Figure 5. Since the phenomenon is most pronounced at higher current rates, the simulation results at the end stages of a 5C discharge were chosen. In the electrolyte subdomain of the $d_s = 1\,\mu$m variant, it can be seen that the lithium concentration close to the anode remains the same as the initial concentration. However, closer to the current collector a depletion of up to 30% is observed. This depletion is caused by the breached pore network resulting from the higher tortuosity, leading to insufficient lithium transport in the electrolyte domain. The diffusion coefficient in the cathode domain is 5 orders of magnitude smaller than the electrolyte domain [38] and [44]. Hence, depletion of lithium close to the current collector in the latter leads to a gradient in the concentration of lithium in the former along the thickness of the cathode as shown in the figure. Similar depletion of lithium in the electrolyte can be observed in the variant $d_s = 2\,\mu$m. Even so, due to lesser depletion in comparison a smaller concentration gradient is observed in the cathode domain. As the CBD diameter further increases, a more homogeneous distribution of lithium and reduced lithium depletion is observed as in the case of variant $d_s = 3\,\mu$m. In contrast, the variant $d_s = 4\,\mu$m exhibits a localized concentration of lithium close to the anode without any evident lithium depletion in the electrolyte. This effect can be attributed to the poor distribution of CBD clusters in the variant. Localized sites that are electrically well-connected to the cathode current collector display higher levels of lithium concentration. Thus, leading to an inhomogeneous distribution.

3.2 | Fractal dimension

Figure 6 shows the complete domain of the investigated idealized geometries for the substudy of fractal dimension. In the figure, a magnified representation of the CBD clusters can be seen. Each of these clusters is described by three characteristics, namely the size of the cluster in the form of the gyration diameter d_g, the size of the individual particles that constitute the cluster denoted by the primary particle size d_p, and the number of primary particles that constitute an individual cluster n_p. The characteristics are linked to the shape of the cluster denoted by its fractal dimension d_f following the relation [27,28]:

$$n_p = k_f \left(\frac{d_g}{d_p} \right)^{d_f}. \tag{8}$$

Herein, k_f represents a proportionality constant. Visual examination of the variants reveals a variation in the fractal dimension d_f as well as the primary particle size d_p of the CBD clusters. Each CBD cluster is assumed to have a gyration diameter of approximately 4 μm. In accordance with Equation (8) with increasing fractal dimension, the number of primary particles that comprise an individual cluster n_p increases from 13 for $d_f = 1.8$ to 28 for $d_f = 2.4$. Consequently, the concentration of mass about the axis of rotation of the CBD cluster increases significantly for the variants with $d_p = 1\,\mu$m. In comparison, for variants with $d_p = 2\,\mu$m the number of primary particles for the same fractal

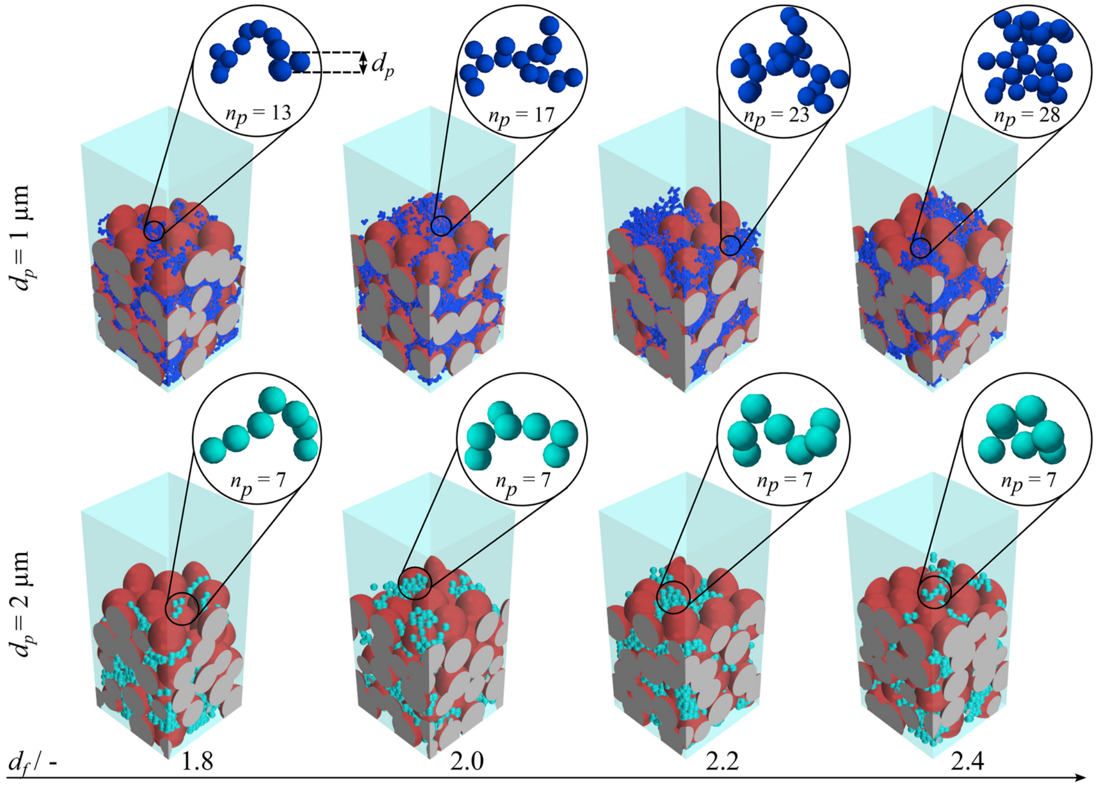

Figure 6 Idealized half-cell geometries of the CBD fractal dimension variants with variation in fractal dimension d_f and primary particle size d_p

dimension decreases. Furthermore, with increasing fractal dimension, the number of primary particles that constitute a single cluster does not change and the mass concentration about the axis of rotation remains unchanged. Since the volume fraction of the CBD content has been kept constant over all the variants, the half geometries with smaller fractal dimensions and smaller primary particle size exhibit higher dispersion of the CBD content as compared to higher fractal dimension and larger primary particle size.

In order to quantify the effect of the changes observed, a similar structural characterization as described in the previous substudy was performed, as depicted by Figure 7. The findings for the variants with $d_p = 1\,\mu$m are plotted in Figure 7a,b . From Figure 7b, it can be observed from the left axis that with changing fractal dimension of the CBD, the tortuosity increases slightly with a maximum change of 6%. Additionally, a gradual but small increase in the electrical conductivity with decreasing fractal dimension can also be observed on the right axis. These changes can be attributed to the higher dispersion levels of CBD content in the cathode geometries with a smaller fractal dimension. Finally, as is observable in Figure 7a, the specific active surface area remains constant over the entire range of the fractal dimension. Figure 7c,d represents the structural characterization of the idealized half-cell geometries with d_p set to 2 μm. In contrast to what was observed previously, it can be seen in Figure 7d from the left axis, that the tortuosity remains constant over the entire range. The influence of decreasing fractal dimension on the effective electrical conductivity also diminishes with an increase in the primary particle size as is seen from the right axis. Similarly, the change in the specific active surface area remains insignificant with a maximum change of 3% as depicted in Figure 7c. A comparison of the structural characterization for the two primary particle sizes, however, reveals more apparent trends. On comparing Figure 7b and 7d, it can be seen that the tortuosity as well as the electrical conductivity increased with decreasing size. Furthermore, a comparison of Figure 7a and 7c reveals a decrease in specific active surface area with smaller primary particle size. These observations are congruent with the influence of size of the CBD clusters in the domain $1 \leq d_s \leq 2\,\mu$m as discussed earlier in Section 3.1. Since a more significant change was observed in the structural characteristics upon change in the primary particle size, it can be inferred that in the investigated domain of half-cells, size has a more significant impact on the structural characteristics and hence the half-cell performance than the fractal dimension.

RESEARCH ARTICLE
doi.org/10.1002/elsa.202100151

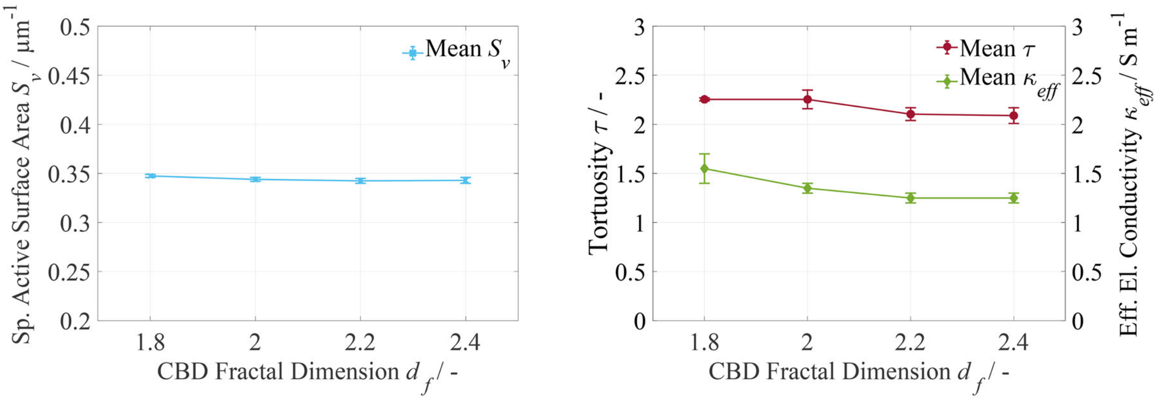

(a) d_p= 1 µm **(b)** d_p= 1 µm

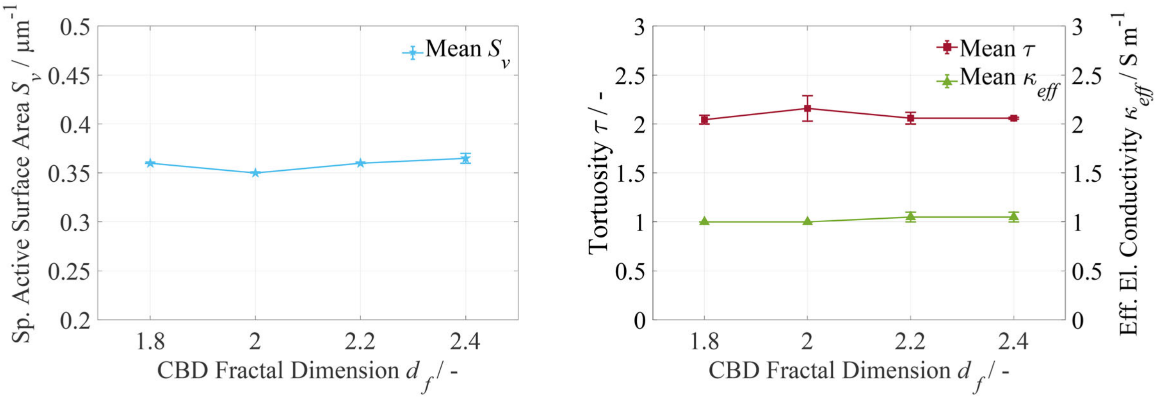

(c) d_p= 2 µm **(d)** d_p= 2 µm

Figure 7 Structural characterization of the CBD fractal dimension variants

Based on the strong link observed between structural characteristic and half-cell performance in the previous substudy, it is to be expected that the performance of the variants is similar to one another due to the insignificant changes in the structural properties across the entire investigated domain. Nonetheless, performance analysis was carried out for the variants with $d_p = 1\,\mu$m. Similar to the CBD size study, the half-cell discharge curves and the utilizable capacities of the variants were examined across different C-rates: 1C, 2C, and 5C. As expected, the discharge curves of the variants were found to lie on one another for the respective discharge rate and the utilizable capacity remained indifferentiable. A decrease in the utilizable capacity with increasing discharge rate for all variants similar to what was seen earlier is also observable in Figure 8b.

In a further attempt to distinguish the fractal dimension variants from one another and to reveal differences on the microstructural level, the lithium distribution field for the cathode and electrolyte domains of the variants was investigated as shown in Figure 9. At a first glance, a strong lithium depletion in the electrolyte domain, as was seen in the case of the smallest size variant in the size substudy, is not observed. Although the investigated variants possess the same particle diameter as the smallest case in the size substudy, wherein high levels of depletion were observed, the investigated thickness of the cathode for the fractal dimension variants is smaller, resulting in reduced tortuosity. Due to the smaller length that the ions need to traverse to reach the farthest limits of the cathode, the ionic conductivity is comparatively better. Moreover, the gradient of lithium concentration in the electrolyte domain remains similar over the variants as can be seen in the figure. Finally, a higher concentration of lithium close to the separator in the active material is observed for all the fractal dimension variants. The apparent inhomogeneous distribution can be accounted for by the inferior structural properties of all the fractal dimension variants in comparison to the size variant with $d_s = 3\,\mu$m, wherein a homogeneous distribution of lithium concentration was seen. The indistinguishable distributions in the cathode domain provide further evidence that the fractal dimension plays a subordinate role on the performance of the investigated half-cells.

4 | CONCLUSION AND OUTLOOK

Within the framework of this publication, various possible particulate cathode microstructures that may arise during

RESEARCH ARTICLE
doi.org/10.1002/elsa.202100151

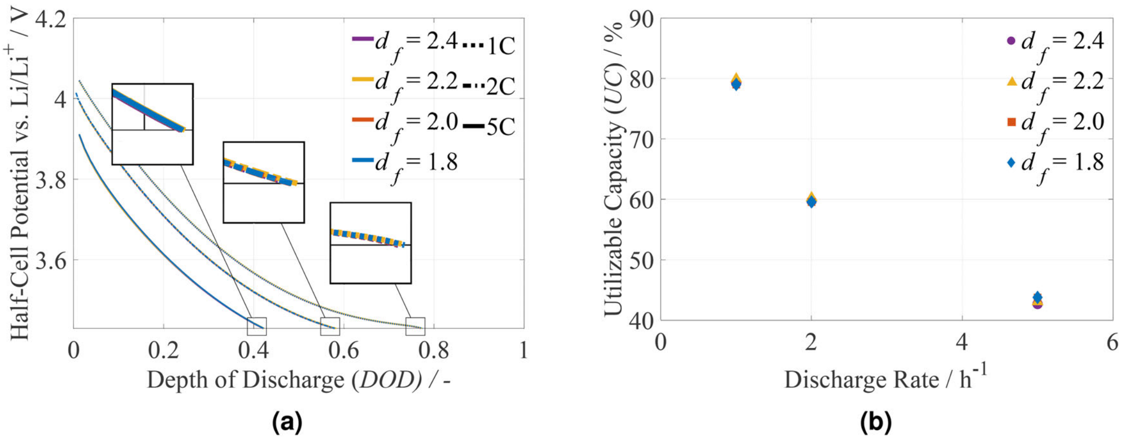

(a) (b)

Figure 8 Performance evaluation of the chosen CBD fractal dimension variants

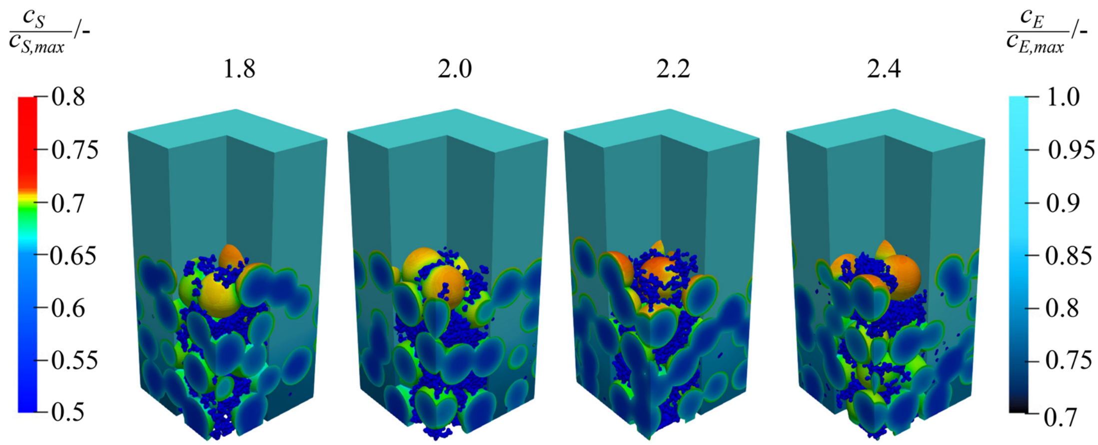

Figure 9 Relative lithium concentration distribution in the cathode and electrolyte domain of the selected CBD fractal dimension variants after 310 s of galvanostatic discharge at 5C

the processes involved in the manufacturing of LIBs were investigated. The microstructures were realized by means of idealized half-cell geometries comprising of an active component (NMC) and a composite passive component composed of carbon black and binder (CBD). The focus of the study was layed on the impact of the size and fractal dimension of the CBD on the structural characteristics and hence performance of the half-cells. The contribution has been divided into two substudies namely size and fractal dimension. For each study at first the computationally generated half-cells were structurally characterized by means of numerical simulations followed by the evaluation of performance using spatially resolved discharge simulations at varying discharge rates.

In the size substudy, contrasting trends in the evolution of electric and ionic conductivity with the CBD size were observed. On the one hand, the tortuosity of the cathode microstructures worsened with reducing CBD size, thus worsening ionic conductivity. On the other hand, electrical conductivity was found to be improved as the CBD clusters became smaller. Hence, the two conduction phenomena are interdependent and can only be improved at the cost of the other. Moreover, an initial increase followed by a sharp decline was observed for the specific active surface area. Hence, it can be concluded that larger CBD clusters $d_s \geq 2\,\mu$m lead to better overall ionic conductivity and the smaller CBD clusters $d_s \leq 1\,\mu$m compromised the ionic conductivity in exchange for increased electrical conductivity. The performance evaluation mirrored the trends observed in the structural characterization thus confirming the considerable impact of structural properties on the half-cell performance. Finally, the trends in the chosen performance metric, that is, utilizable capacity, indicates a shift in the performance-dominating phenomenon with increasing discharge rate. As is evident by the declining difference in the *UC* of the variants with increasing discharge rate, the structural properties of the cathode microstructure play a more crucial role at smaller discharge rates but with increasing demands of current at higher discharge rates further loss mechanisms such as depletion of electrolyte close to the current collector and solid-state diffusion limitation become more significant. In the fractal dimension substudy, the fractal dimension as well as the primary particle size was varied. Unlike the size substudy, no significant change in the structural properties was seen with variation in the fractal dimension. However, upon an increase in the size of the primary particles constituting the individual clusters similar trends as observed in the size substudy were noticed. Thus, it can be concluded that within the investigated range of size and fractal dimension, the size of the CBD clusters plays a more pronounced role in the performance of half-cells. Therefore, it is imperative to account for the size of CBD clusters while manufacturing tailored LIB cathodes to be used in high-energy and high-power applications, respectively.

In this contribution, the CBD clusters were considered to be dense spheres. However, the CBD has been found to be nanoporous in recent research work. Inclusion of the CBD nanoporosity will significantly impact the ionic diffusion within the half-cell. Hence, it is a lucrative avenue for extension of the model currently presented in this work. Furthermore, the extension of the study to even smaller particles sizes and a larger span of fractal dimension with comprehensive variation in the structural parameters as well as the incorporation of particle distributions in cathode slurries remains a topic of ongoing research.

ACKNOWLEDGMENTS

The authors gratefully acknowledge the funding and support by the German Research Foundation (DFG - Deutsche Forschungsgemeinschaft) within the research training group SiMET under the project number DFG GRK 2218/2. Additionally, the support by the state of Baden-Württemberg through bwHPC is highly acknowledged. Finally, the authors would like to thank Rafdian Nahri for his assistance in carrying out numerical simulations.

CONFLICT OF INTEREST

The authors declare no conflict of interest.

DATA AVAILABILITY STATEMENT

The data that support the findings of this study are available from the corresponding author upon reasonable request.

ORCID

Anshuman Chauhan https://orcid.org/0000-0002-4871-178X
Ermek Asylbekov https://orcid.org/0000-0002-2118-1782
Susanne Kespe https://orcid.org/0000-0001-6538-7427

REFERENCES

1. R. Amin, Y.-M. Chiang, *J. Electrochem. Soc.* **2016**, *163*, A1512.
2. W. Bauer, D. Nötzel, V. Wenzel, H. Nirschl, *J. Power Sources* **2015**, *288*, 359.
3. E. N. Primo, M. Chouchane, M. Touzin, P. Vazquez, A. A. Franco, *J. Power Sources* **2021**, *488*, 229361.
4. G. Ambrosetti, N. Johner, C. Grimaldi, T. Maeder, P. Ryser, A. Danani, *J. Appl. Phys.* **2009**, *106*, 016103.
5. M. Q. Zhang, J. R. Xu, H. M. Zeng, Q. Huo, Z. Y. Zhang, F. C. Yun, K. Friedrich, *J. Mater. Sci.* **1995**, *30*, 4226.
6. K. Miyasaka, K. Watanabe, E. Jojima, H. Aida, M. Sumita, K. Ishikawa, *J. Mater. Sci.* **1982**, *17*, 1610.
7. A. Awarke, S. Lauer, S. Pischinger, M. Wittler, *J. Power Sources* **2011**, *196*, 405.
8. D. Guy, B. Lestriez, R. Bouchet, D. Guyomard, *J. Electrochem. Soc.* **2006**, *153*, A679.
9. L. Almar, J. Joos, A. Weber, E. Ivers-Tiffée, *J. Power Sources* **2019**, *427*, 1.
10. T.-T. Nguyen, J. Villanova, Z. Su, R. Tucoulou, B. Fleutot, B. Delobel, C. Delacourt, A. Demortière, *Adv. Energy Mater.* **2021**, *11*, 2003529.
11. B. L. Trembacki, A. N. Mistry, D. R. Noble, M. E. Ferraro, P. P. Mukherjee, S. A. Roberts, *J. Electrochem. Soc.* **2018**, *165*, E725.
12. S. Hein, T. Danner, D. Westhoff, B. Prifling, R. Scurtu, L. Kremer, A. Hoffmann, A. Hilger, M. Osenberg, I. Manke, M. Wohlfahrt-Mehrens, V. Schmidt, A. Latz, *J. Electrochem. Soc.* **2020**, *167*, 013546.
13. A. Shodiev, E. N. Primo, M. Chouchane, T. Lombardo, A. C. Ngandjong, A. Rucci, A. A. Franco, *J. Power Sources* **2020**, *454*, 227871.
14. M. Park, X. Zhang, M. Chung, G. B. Less, A. M. Sastry, *J. Power Sources* **2010**, *195*, 7904.
15. G. Inoue, M. Kawase, *J. Power Sources* **2017**, *342*, 476.
16. Y.-H. Chen, C.-W. Wang, G. Liu, X.-Y. Song, V. S. Battaglia, A. M. Sastry, *J. Electrochem. Soc.* **2007**, *154*, A978.
17. Y.-H. Chen, C.-W. Wang, X. Zhang, A. M. Sastry, *J. Power Sources* **2010**, *195*, 2851.
18. J. K. Mayer, L. Almar, E. Asylbekov, W. Haselrieder, A. Kwade, A. Weber, H. Nirschl, *Energy Technol.* **2020**, *8*, 1900161.
19. L. S. Kremer, A. Hoffmann, T. Danner, S. Hein, B. Prifling, D. Westhoff, C. Dreer, A. Latz, V. Schmidt, M. Wohlfahrt-Mehrens, *Energy Technol.* **2020**, *8*, 1900167.
20. H. Dreger, M. Huelsebrock, L. Froboese, A. Kwade, *Ind. Eng. Chem. Res.* **2017**, *56*, 2466.
21. E. Asylbekov, R. Trunk, M. J. Krause, H. Nirschl, *Energy Technol.* **2021**, 2000850.
22. M. M. Forouzan, C.-W. Chao, D. Bustamante, B. A. Mazzeo, D. R. Wheeler, *J. Power Sources* **2016**, *312*, 172.
23. A. Rucci, A. C. Ngandjong, E. N. Primo, M. Maiza, A. A. Franco, *Electrochim. Acta* **2019**, *312*, 168.
24. A. C. Ngandjong, T. Lombardo, E. N. Primo, M. Chouchane, A. Shodiev, O. Arcelus, A. A. Franco, *J. Power Sources* **2021**, *485*, 229320.
25. I. Srivastava, D. S. Bolintineanu, J. B. Lechman, S. A. Roberts, *ACS Appl. Mater. Interfaces* **2020**, *12*, 34919.
26. A. C. Ngandjong, A. Rucci, M. Maiza, G. Shukla, J. Vazquez-Arenas, A. A. Franco, *J. Phys. Chem. Lett.* **2017**, *8*, 5966.
27. U. Kätzel, R. Bedrich, M. Stintz, R. Ketzmerick, T. Gottschalk-Gaudig, H. Barthel, *Part. Part. Syst. Charact.* **2008**, *25*, 9.

28. S. R. Forrest, T. A. Witten, *J Phys. A: Math. Gen.* **1979**, *12*, L109.
29. C. Kloss, C. Goniva, A. Hager, S. Amberger, S. Pirker, *Prog. Comput. Fluid Dyn, Int J.* **2012**, *12*, 140.
30. R. D. Mindlin, *J. Appl. Mech.* **1949**, *16*, 259.
31. M. A. Kespe, Simulation von transportvorgängen in lithiumionen batterien auf der partikulären ebene, Karlsruhe Institute of Technology (in German).
32. D.-W. Chung, M. Ebner, D. R. Ely, V. Wood, R. Edwin García, *Modell. Simul. Mater. Sci. Eng.* **2013**, *21*, 074009.
33. D. Kehrwald, P. R. Shearing, N. P. Brandon, P. K. Sinha, S. J. Harris, *J. Electrochem. Soc.* **2011**, *158*, A1393.
34. M. Kespe, H. Nirschl, *Int. J. Energy Res.* **2015**, *39*, 2062.
35. M. Kespe, M. Gleiß, S. Hammerich, H. Nirschl, *Int. J. Energy Res.* **2017**, *41*, 2282.
36. M. Kespe, S. Cernak, M. Gleiß, S. Hammerich, H. Nirschl, *Int. J. Energy Res.* **2019**.
37. S. Cernak, F. Schuerholz, M. Kespe, H. Nirschl, *Energy Technol.* **2020**, 2000676.
38. S. Cernak, F. Gerbig, M. Kespe, H. Nirschl, *Energy Storage* **2020**, *2*, 5.
39. G. B. Less, J. H. Seo, S. Han, A. M. Sastry, J. Zausch, A. Latz, S. Schmidt, C. Wieser, D. Kehrwald, S. Fell, *J. Electrochem. Soc.* **2012**, *159*, A697.
40. J. Newman, K. E. Thomas-Alyea, *Electrochemical Systems*, 3rd ed. Wiley-Interscience, Hoboken, NJ, **2012**.
41. J. Vetter, P. Novák, M. R. Wagner, C. Veit, K.-C. Möller, J. O. Besenhard, M. Winter, M. Wohlfahrt-Mehrens, C. Vogler, A. Hammouche, *J. Power Sources* **2005**, *147*, 269.
42. S. Pejovnik, R. Dominko, M. Bele, M. Gaberscek, J. Jamnik, *J. Power Sources* **2008**, *184*, 593.
43. W. Du, A. Gupta, X. Zhang, A. M. Sastry, W. Shyy, *Int. J. Heat Mass Transfer* **2010**, *53*, 3552.
44. F. M. Kindermann, A. Noel, S. V. Erhard, A. Jossen, *Electrochim. Acta* **2015**, *185*, 107.

How to cite this article: Chauhan A, Asylbekov E, Kespe S, Nirschl H. Influence of carbon binder domain on the performance of lithium-ion batteries: Impact of size and fractal dimension. *Electrochem Sci Adv*. **2022**; e2100151. https://doi.org/10.1002/elsa.202100151